



ARTICLE

Isogeometric Boundary Element Method for Two-Dimensional Steady-State Non-Homogeneous Heat Conduction Problem

Yongsong Li¹, Xiaomeng Yin² and Yanming Xu^{1,*}

¹School of Architectural Engineering, Huanghuai University, Zhumadian, 463000, China

²College of Intelligent Construction, Wuchang University of Technology, Wuhan, 430223, China

*Corresponding Author: Yanming Xu. Email: xuyanming@ustc.edu

Received: 10 November 2021 Accepted: 08 January 2022

ABSTRACT

The isogeometric boundary element technique (IGABEM) is presented in this study for steady-state inhomogeneous heat conduction analysis. The physical unknowns in the boundary integral formulations of the governing equations are discretized using non-uniform rational B-spline (NURBS) basis functions, which are utilized to build the geometry of the structures. To speed up the assessment of NURBS basis functions, the Bézier extraction approach is used. To solve the extra domain integrals, we use a radial integration approach. The numerical examples show the potential of IGABEM for dimension reduction and smooth integration of CAD and numerical analysis.

KEYWORDS

Isogeometric analysis; NURBS; boundary element method; heat conduction; non-homogeneous; radial integration method

1 Introduction

Isogeometric analysis (IGA) has garnered considerable attention in engineering research since Hughes' pioneering study [1]. IGA employs spline functions for geometric expressions in CAD, such as non-uniform rational B-spline (NURBS) as basis functions to approximate unknown physics fields as an alternative to the usual numerical techniques based on Lagrange polynomials. IGA offers high-order consistency and versatile refinement strategies, which are very appealing in numerical simulations. IGA has been effectively implemented in numerous sectors owing to various advantages as described next [2–6]. The Bézier [7] extraction procedure has been used to increase the simulation performance and make it easier to apply IGA. Although the notion of IGA was initially established in the context of the finite element technique, its implementation in engineering practice is limited owing to its reliance on volume parameterization, which is incompatible with the boundary representation of CAD. However, the boundary element method (BEM) requires boundary parameterization and is inherently compatible with CAD models. The isogeometric boundary element method (IGABEM) has been effectively applied to a variety of



domains, including linear elasticity [8–11], potential problems [12–14], fracture mechanics [15–18], electromagnetics [19], acoustics [20–29], and structural optimization [30–35], and others.

In this study, we use the NURBS method to construct a two-dimensional isogeometric model. The Bézier curve, proposed by Pierre Bézier in 1962, paved the path for the application of spline functions for modeling curved surfaces. The application of spline functions in curved surface modeling has been initiated, and NURBS has become the most widely used modeling tool in geometric modeling in the past few decades. NURBS has outstanding advantages for curved surface modeling. It can accurately represent quadratic curved surfaces, thus providing a uniform mathematical representation of regular and free surfaces. It includes a weight factor that affects the shape of curved surfaces, making it easier to control and achieve the required shape.

In this study, we focus on the heat conduction problem. Many researchers have used traditional methods to solve heat conduction problems, such as the singular boundary method for steady-state nonlinear heat conduction problems with temperature-dependent thermal conductivity [36], the combination of the BEM and radial basis function method (RBF) for the evaluation of domain integrals with boundary-only discretization [37,38], IGABEM based on NURBS for 3D steady-state thermal conduction problems for a medium with non-homogeneous inclusions [39,40], and for solving transient heat conduction problems with heat sources [41–46]. The subtraction of singularity technique is applied to compute the singular integrals in the BEM [47]. Subsequently, we have coupled RBF and IGABEM for problems of steady heat conduction with variable coefficients. RBF is used to transform the domain integral generated by variable thermal conductivity parameters and the source term into a boundary integral. The operation enables full utilization of the advantages of IGABEM with NURBS.

The remainder of this paper is organized as follows. Section 2 describes the NURBS basis functions with B-spline functions. In Section 3, the basic theory of steady-state heat conduction is described, and in Section 4, the specific operations of the domain integration treatment and the formulation of the system equations for the iterative solution are detailed. In Section 5, several numerical examples of geometric models constructed by NURBS are discussed to verify the correctness of the algorithm. Finally, the conclusions of this study are summarized in Section 6.

2 NURBS

The principles of NURBS are briefly discussed in this section for completeness. The basis functions of NURBS are defined over a knot vector, which is a monotonic growing real number sequence, represented by $U = \{u_1, u_2, \dots, u_m\}$, where u_i is the i -th knot in vector U . Iteratively, the B-spline basis function is evaluated as Eq. (1):

$$N_{i,p}(u) = \begin{cases} 1, & \text{if } u_i \leq u < u_{i+1}, \\ 0, & \text{otherwise} \end{cases}, \quad p = 0 \quad (1)$$

When $p \neq 0$, we have the expression for $N_{i,p}$, as Eq. (2):

$$N_{i,p}(u) = \frac{u - u_i}{u_{i+p} - u_i} N_{i,p-1}(u) + \frac{u_{i+p+1} - u}{u_{i+p+1} - u_{i+1}} N_{i+1,p-1}(u) \quad (2)$$

In Eqs. (1) and (2), p denotes the rank of the polynomial in the B-spline basis functions.

The derivative of the basis function can be written as Eq. (3):

$$N'_{i,p}(u) = \frac{p}{u_{i+p} - u_i} N_{i,p-1}(u) - \frac{p}{u_{i+p+1} - u_{i+1}} N_{i+1,p-1}(u) \quad (3)$$

The linear combination of NURBS basis functions and the related control points describes the B-spline curve as Eq. (4):

$$\mathbf{x}(u) = \sum_{i=1}^n N_{i,p}(u) \mathbf{P}_i \quad (4)$$

where, \mathbf{P}_i are the Cartesian coordinates of control points.

The weight coefficient ω is used to rationalize the B-spline basis, resulting in non-uniform rational B-spline (NURBS) basis functions as Eq. (5):

$$R_{i,p}(u) = \frac{N_{i,p}(u)\omega_i}{W(u)} \quad (5)$$

where we have the expression for W as shown in Eq. (6):

$$W(u) = \sum_{j=1}^n N_{j,p}\omega_j \quad (6)$$

Similar to B-spline, the NURBS curve is expressed as Eq. (7):

$$\mathbf{x}(u) = \sum_{i=1}^n R_{i,p}(u) \mathbf{P}_i \quad (7)$$

The rational form of the NURBS basis function, which consists of the B-spline basis function plus the weight factor ω , allows the precise description of conic curves such as ellipses and circles.

3 Integral Equations for Steady-State Inhomogeneous Heat Conduction Problems

For most materials, the thermal conductivity varies with temperature. For example, the thermal conductivity of a certain composite material at room temperature is 10.85 W/(m · K), at 200 K and 400 K, its thermal conductivity could be 17.73 W/(m · K) and 20.16 W/(m · K), respectively. If the thermal conductivity is a function of temperature, the control equation is a nonlinear partial differential equation, and we study the BEM for steady-state inhomogeneous heat conduction problems.

The steady-state heat transfer equation for an isotropic medium containing an internal heat source with temperature-dependent thermal conductivity is expressed as Eq. (8):

$$\frac{\partial}{\partial x_i} \left[k(T(\mathbf{x})) \frac{\partial T(\mathbf{x})}{\partial x_i} \right] + Q(\mathbf{x}) = 0 \quad (\mathbf{x} \in \Omega) \quad (8)$$

In Eq. (8), the thermal conductivity $k(T(\mathbf{x}))$ is a function of temperature $T(\mathbf{x})$, $T(\mathbf{x})$ is a function of the coordinates of point \mathbf{x} , $Q(\mathbf{x})$ indicates the value of the heat source at point \mathbf{x} ,

and x_i is the coordinate component of point \mathbf{x} . The boundary conditions are shown in Eqs. (9), (10) and (11):

$$T(\mathbf{x}) = \bar{T}(\mathbf{x}) \quad (\mathbf{x} \in \Gamma_T) \quad (9)$$

$$q(\mathbf{x}) = -k(T(\mathbf{x})) \frac{\partial T(\mathbf{x})}{\partial \mathbf{n}(x)} = \bar{q}(\mathbf{x}) \quad (\mathbf{x} \in \Gamma_q) \quad (10)$$

$$q(\mathbf{x}) = h[T(\mathbf{x}) - T_f(\mathbf{x})] + \varepsilon\sigma [T^4(\mathbf{x}) - T_f^4(\mathbf{x})] \quad (\mathbf{x} \in \Gamma_{Tq}) \quad (11)$$

In Eq. (9), Γ_T indicates a constant temperature boundary; Γ_q in Eq. (10) denotes a constant temperature flux boundary, and $\mathbf{n}(x)$ is the direction vector of the unit outer normal at the boundary point. Eq. (11) is a mixed boundary condition. Now, we introduce the weight function \tilde{G} and the weighted residual operation and divisional integration operation, which can be expressed as Eq. (12):

$$\int_{\Omega} \tilde{G} \frac{\partial}{\partial x_i} \left(k \frac{\partial T}{\partial x_i} \right) d\Omega + \int_{\Omega} \tilde{G} Q d\Omega = 0 \quad (12)$$

Applying the divisional integration method and Gaussian scattering theorem to the first term, we get Eq. (13):

$$\int_{\Omega} \tilde{G} \frac{\partial}{\partial x_i} \left(k \frac{\partial T}{\partial x_i} \right) d\Omega = - \int_{\Gamma} k \frac{\partial T}{\partial x_i} n_i d\Gamma - \int_{\Gamma} k T q^* d\Gamma + \int_{\Omega} T \frac{\partial \tilde{G}}{\partial x_i} \frac{\partial k}{\partial x_i} d\Omega - k(T(y)) T(y) d\Omega \quad (13)$$

Considering the case where the source point p is on the boundary containing the field point q , we may write Eq. (14):

$$\begin{aligned} c(p)k(T(p))T(p) &= - \int_{\Gamma} \tilde{G}(Q,p)q(Q)d\Gamma(Q) - \int_{\Gamma} \frac{\partial \tilde{G}}{\partial x_i} k(T(Q))T(Q)d\Gamma(Q) \\ &+ \int_{\Omega} \tilde{G}(q,p)b(q)d\Omega(q) + \int_{\Omega} \tilde{G}_{,i}(q,p)k_{,i}(T(q))T(q)d\Omega(q) \end{aligned} \quad (14)$$

4 Analytic Expressions for the Conversion of Domain Integrals to Boundary Integrals

Two domain integrals and two boundary integrals appear in the unified equation. The boundary integrals can be calculated directly by discretizing the Gauss-Legendre quadrature. However, the latter two domain integrals are due to the nonlinear thermal conductivity and heat source terms, respectively. For the domain integrals from the nonlinear thermal conductivity, as the integrals contain $k_{,i}T = \frac{\partial k}{\partial x_i}T$, interpolation approximation substitution is needed using radial basis functions and primary polynomials. For integration due to the heat source term, we can use the radial integration method to convert the coordinate representation. Therefore, we focus on the domain integrals due to thermal conductivity nonlinearity and the heat source term.

4.1 Treatment of Domain Integration Due to Thermal Conductivity Nonlinearity

We use radial basis functions and primary polynomials to represent $k_{,i}T$, which is $\frac{\partial k}{\partial x_i}T$, as shown in Eqs. (15) and (16):

$$\frac{\partial k(T(x))}{\partial x_i}T(x) = \sum_{A=1}^{N_A} \alpha_i^A \phi^A(R) + a_i^0 + \sum_{k=1}^{\beta} a_i^k x_k \tag{15}$$

$$\sum_{A=1}^{N_A} \alpha_i^A = \sum_{A=1}^{N_A} \alpha_i^A x_k^A = 0 \tag{16}$$

Here, α_i^A , a_i^0 and a_i^k are the coefficients to be determined, $\phi^A(R)$ is the radial basis function, which is a most commonly used function, as shown in Table 1.

Table 1: Common radial basis functions

NTYP	1	2	3	4	5	6
$\phi^A(R)$	$2R(1 + 2 \ln R)$	$-2Re^{-R^2}$	$\frac{R}{\sqrt{R^2+c^2}}$	$\frac{-R}{\sqrt[3]{R^2+c^2}}$	$20R(R-1)^3$	$12R(R-1)^2$

By applying the radial basis function in Eqs. (15) and (16) to all nodes, we obtain a set of algebraic equations written in matrix form as Eq. (17):

$$\{k_{,i}T\} = \mathbf{f}\alpha_i \tag{17}$$

where α_i is the column vector consisting of the coefficients. Matrix \mathbf{f} is written as Eq. (18):

$$\mathbf{f} = \begin{bmatrix} f^{11} & f^{12} & \dots & f^{1N} & 1 \mathbf{x}_1^1 \mathbf{x}_2^1 & \mathbf{x}_1^1 \mathbf{x}_2^1 & \mathbf{x}_1^1 \mathbf{x}_2^1 & \mathbf{x}_1^1 \mathbf{x}_2^1 & \mathbf{x}_2^1 \mathbf{x}_1^1 & \mathbf{x}_2^1 \mathbf{x}_1^1 \\ f^{21} & f^{22} & \dots & f^{2N} & 1 \mathbf{x}_1^2 \mathbf{x}_2^2 & \mathbf{x}_1^2 \mathbf{x}_2^2 & \mathbf{x}_1^2 \mathbf{x}_2^2 & \mathbf{x}_1^2 \mathbf{x}_2^2 & \mathbf{x}_2^2 \mathbf{x}_1^2 & \mathbf{x}_2^2 \mathbf{x}_1^2 \\ \vdots & \vdots & & \vdots \\ f^{N1} & f^{N2} & \dots & f^{NN} & 1 \mathbf{x}_1^N \mathbf{x}_2^N & \mathbf{x}_1^N \mathbf{x}_2^N & \mathbf{x}_1^N \mathbf{x}_2^N & \mathbf{x}_1^N \mathbf{x}_2^N & \mathbf{x}_2^N \mathbf{x}_1^N & \mathbf{x}_2^N \mathbf{x}_1^N \\ 1 & 1 & \dots & 1 & 0 & 0 & 0 & 0 & 0 & 0 \\ \mathbf{x}_1^1 & \mathbf{x}_1^2 & \dots & \mathbf{x}_1^N & 0 & 0 & 0 & 0 & 0 & 0 \\ \mathbf{x}_2^1 & \mathbf{x}_2^2 & \dots & \mathbf{x}_2^N & 0 & 0 & 0 & 0 & 0 & 0 \\ \mathbf{x}_1^1 \mathbf{x}_2^1 \mathbf{x}_1^2 \mathbf{x}_2^2 \dots \mathbf{x}_1^N \mathbf{x}_2^N & 0 & 0 & 0 & 0 & 0 & 0 & 0 & 0 & 0 \\ \mathbf{x}_1^1 \mathbf{x}_1^1 \mathbf{x}_2^2 \mathbf{x}_1^2 \dots \mathbf{x}_1^N \mathbf{x}_1^N & 0 & 0 & 0 & 0 & 0 & 0 & 0 & 0 & 0 \\ \mathbf{x}_2^1 \mathbf{x}_2^1 \mathbf{x}_2^2 \mathbf{x}_2^2 \dots \mathbf{x}_2^N \mathbf{x}_2^N & 0 & 0 & 0 & 0 & 0 & 0 & 0 & 0 & 0 \end{bmatrix} \tag{18}$$

The matrix is invertible under the condition that no nodes overlap, and this is obtained by the chain rule shown in Eq. (19):

$$\alpha_i = \mathbf{f}^{-1} \left\{ \frac{\partial k}{\partial T} \frac{\partial T}{\partial x_i} T \right\} \tag{19}$$

where $\frac{\partial T}{\partial x_i}$ is the value of the derivative of the unknown temperature at the node, which can be solved by the integral equation method or by performing an augmented basis function expression approximation. We have the expression for $T(x)$, as shown in Eqs. (20) and (21):

$$T(x) = \sum_{A=1}^{N_A} \alpha^A \phi^A(R) + a^0 + \sum_{k=1}^{\beta} a^k x_k \quad (20)$$

$$\sum_{A=1}^{N_A} \alpha^A = \sum_{A=1}^{N_A} \alpha^A x_k^A = 0 \quad (21)$$

The temperature gradient can be expressed as Eq. (22):

$$\frac{\partial T(x)}{\partial x_i} = \sum_A^{N_A} \alpha^A \frac{\partial \phi^A(R)}{\partial R} \frac{\partial R}{\partial x_i} + a^i \quad (22)$$

in which $\frac{\partial \phi^A(R)}{\partial R}$ denotes the derivative of the radial basis function with respect to R , as shown in Table 2. We can write the expressions for R and its partial derivative with respect to x_i , as shown in Eqs. (23) and (24):

$$R = \sqrt{(x_i - x_i^A)(x_i - x_i^A)} \quad (23)$$

$$\frac{\partial R}{\partial x_i} = \frac{x_i - x_i^A}{R} \quad (24)$$

Table 2: The derivatives of the common radial basis functions with respect to R

NTYP	A	B	C	D	E	F
$\frac{\partial \phi^A(R)}{\partial R}$	$2R(1 + 2 \ln R)$	$-2R e^{-R^2}$	$\frac{R}{\sqrt{R^2 + c^2}}$	$\frac{-R}{\sqrt[3]{R^2 + c^2}}$	$20R(R - 1)^3$	$12R(R - 1)^2$

In Eqs. (20) and (21), the coefficients to be determined can be obtained from the collocation of the boundary and interior points, and the matrix equation can be written as Eq. (25):

$$\alpha = \mathbf{f}^{-1} T \quad (25)$$

In Eq. (25), the column vector of the temperature at each point can be calculated using the value of the previous iteration, and the last term of the domain integral of Eq. (14) is approximated by substitution using the radial integration method. Hence, we may write Eq. (26):

$$\begin{aligned}
 & \int_{\Omega} \tilde{G}_{,i}(q,p)k_{,i}(T(q))T(q)d\Omega(q) \\
 &= \int_{\Omega} \tilde{G}_{,i}(q,p)k_{,i}(T(q)) \left(\sum_{A=1}^{N_A} \alpha_i^A \phi^A(R) + a_i^0 + \sum_{k=1}^{\beta} a_i^k x_k \right) d\Omega(q) \\
 &= A + B + C
 \end{aligned} \tag{26}$$

and Eq. (27):

$$\begin{cases}
 A = \sum_{A=1}^{N_A} \alpha_i^A \int_{\Omega} \tilde{G}_{,i}(q,p)k_{,i}(T(q))\phi^A(R)d\Omega(q) \\
 B = a_i^0 \int_{\Omega} \tilde{G}_{,i}(q,p)k_{,i}(T(q))d\Omega(q) \\
 C = \sum_{k=1}^{\beta} a_i^k \int_{\Omega} \tilde{G}_{,i}(q,p)k_{,i}(T(q))x_k d\Omega(q)
 \end{cases} \tag{27}$$

We continue the simplification of the equation of C in Eq. (27), as shown in Eq. (28):

$$\begin{aligned}
 C &= \sum_{k=1}^{\beta} a_i^k \int_{\Omega} \tilde{G}_{,i}(q,p)k_{,i}(T(q)) [(x_k - x_p) + x_p] d\Omega(q) \\
 &= \sum_{k=1}^{\beta} a_i^k \int_{\Omega} \tilde{G}_{,i}(q,p)k_{,i}(T(q)) [(x_k - x_p)] d\Omega(q) + \sum_{k=1}^{\beta} a_i^k \int_{\Omega} \tilde{G}_{,i}(q,p)k_{,i}(T(q))x_p d\Omega(q)
 \end{aligned} \tag{28}$$

The original equation is thus obtained by simplifying and combining similar terms as Eq. (29):

$$\begin{aligned}
 \int_{\Omega} \tilde{G}_{,i}(q,p)k_{,i}(q)T(q)d\Omega(q) &= \alpha_i^A \int_{\Gamma} \frac{1}{r^\alpha(Q,p)} \frac{\partial r}{\partial n} F_i^A(Q,p) d\Gamma(q) \\
 &+ a_i^k \int_{\Gamma} \frac{r_{,k}}{r^\alpha(Q,p)} \frac{\partial r}{\partial n} F_i^1(Q,p) d\Gamma(q) \\
 &+ (a_i^k x_k^p + a_i^0) \int_{\Gamma} \frac{1}{r^\alpha(Q,p)} \frac{\partial r}{\partial n} F_i^0(Q,p) d\Gamma(q)
 \end{aligned} \tag{29}$$

in which, we have Eq. (30):

$$\begin{aligned}
 F_i^A(Q,p) &= \int_0^{r(Q,p)} \tilde{G}_{,i}(q,p)\phi^A r^\alpha dr = \frac{-r_{,i}}{2\pi\alpha} \int_0^{r(Q,p)} \phi^A dr(q) \\
 F_i^1(Q,p) &= \int_0^{r(Q,p)} \tilde{G}_{,i}(q,p)r^{\alpha+1} dr = \frac{-r_{,i}r^2(Q,p)}{4\pi\alpha} \\
 F_i^0(Q,p) &= \int_0^{r(Q,p)} \tilde{G}_{,i}(q,p)r^\alpha dr = \frac{-r_{,i}r(Q,p)}{2\pi\alpha}
 \end{aligned} \tag{30}$$

The Gaussian product formula is used to solve the radial integral analytically for the inverse complex quadratic radial basis function, which is usually in the form of a tight branch, as shown in Eq. (31):

$$\phi^A(R) = \begin{cases} \frac{1}{\sqrt{\left(\frac{R}{d_A}\right)^2 + c^2}} & (0 \leq R < d_A) \\ 0 & (d_A \leq R) \end{cases} \quad (31)$$

It can be noted that $\phi^A(R)$ is invalid for points outside the compactly supported radius. Eq. (31) can be solved radially by substituting into Eq. (30). The computation of radial integrals by numerical methods is time consuming and can be improved by the analytical solution of Eq. (30).

For Eq. (31), we use the radial integration method for the analytical solution, as shown in Eq. (32):

$$\int_0^r \phi^A dr = \int_{r_1}^{r_2} \phi^A dr = \int_{r_1}^{r_2} \frac{1}{\sqrt{\left(\frac{R}{d_A}\right)^2 + c^2}} dr = \left(\ln \left| \sqrt{1 + \left(\frac{R}{d_A}\right)^2} + \frac{R}{d_A} \right| \right) / d_A^2 \Big|_{r_1}^{r_2} \quad (32)$$

Fig. 1 shows the radial integration distance diagram. For a few special cases, the source point, field point, and action point are in a straight line as shown in Fig. 2. In such cases, we can solve Eq. (32) analytically. In the radial basis division method, the use of numerical integration requires considerable time, while the use of analytical solutions (as in Eq. (30)), can improve the efficiency of the calculation by several times.

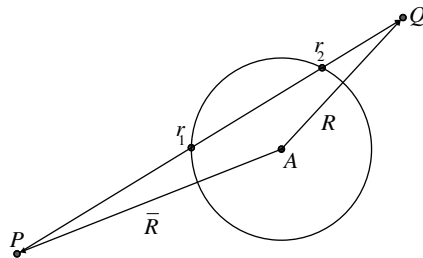


Figure 1: Schematic diagram of the starting and ending distances of radial integration

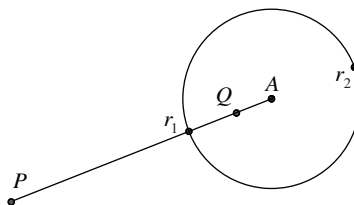


Figure 2: Special case where the tightly-supported domain intersects the radius

4.2 Processing of Domain Integrals Caused by Source Terms

We first consider the domain integral for the heat source, which is the third term on the right hand side of Eq. (14). By using the radial basis function method, the following expression can be obtained because the boundary integral can be calculated directly by Gaussian integration. We only need to consider the treatment of the domain integral. First, we consider the domain integral owing to the heat source, i.e., the second term on the right-hand side of Eq. (13) is treated using the radial basis method, and the following expression can be obtained as Eq. (33):

$$\left(\tilde{G}(q,p)b(q)\right)(\mathbf{x}) := \int_{\Gamma} \frac{B(\mathbf{x},\mathbf{y})}{r(\mathbf{x},\mathbf{y})} \frac{\partial r}{\partial \mathbf{n}(\mathbf{y})} d\Gamma(\mathbf{y}) \quad (33)$$

where $B(\mathbf{x},\mathbf{y})$ is the basis function obtained from the heat source function after the radial basis method and is expressed as Eq. (34):

$$B(\mathbf{x},\mathbf{y}) = \int_0^{r(\mathbf{x},\mathbf{y})} G(\mathbf{x},\tilde{\mathbf{y}}) Q(\tilde{\mathbf{y}}) r^2(\mathbf{x},\tilde{\mathbf{y}}) dr(\tilde{\mathbf{y}}) \quad (34)$$

We have considered a three-dimensional problem here. Therefore, the power of r is $3-1=2$. A specific derivation method can be observed in the radial basis partition. For simple heat source distribution functions, the basis function B can be derived analytically, and for complex heat source distribution functions, it can be approximated by Gaussian numerical integration.

4.3 The Set of System Equations

The unified integral boundary is discretized into N_e boundary cells, the number of boundary nodes is N_b , and the domain has N_i points. The total number of nodes is $N_A = N_b + N_e$, N_A nodes are considered as the source p in turn, and the domain integral matrix equation can be calculated, as Eq. (35):

$$\int_{\Omega} \tilde{G}_{,i}(q,p) k_{,i}(q,p) T(q) d\Omega(q) = \mathbf{F}\alpha_i \quad (35)$$

Substituting Eq. (25) into Eq. (35), we obtain Eq. (36):

$$\int_{\Omega} \tilde{G}_{,i}(q,p) k_{,i}(q,p) T(q) d\Omega(q) = \mathbf{F}_i \mathbf{f}^{-1} \left\{ \frac{\partial k}{\partial T} \frac{\partial T}{\partial x_i} T \right\} \quad (36)$$

Finally, a unified system of algebraic equations is obtained, as shown in Eq. (37):

$$H(kT) - Gq = y_b + \mathbf{F}_i \mathbf{f}^{-1} \left\{ \frac{\partial k}{\partial T} \frac{\partial T}{\partial x_i} T \right\} \quad (37)$$

$\mathbf{F}_i \mathbf{f}^{-1}$ indicates that the elements of the matrix are temperature dependent. The system equations are then obtained by imposing the boundary conditions in Eqs. (9) and (10), and we obtain the system of equations as Eq. (38):

$$\mathbf{A}\mathbf{X} + \mathbf{B} = \mathbf{Y} \quad (38)$$

In Eq. (38), \mathbf{A} denotes the elements in matrix \mathbf{A} as a function of temperature T , \mathbf{X} is a column vector consisting of all unknown node temperatures and unknown boundary fluxes, matrix \mathbf{B} has values only at the node positions corresponding to the thermal radiation boundary conditions, and the elements at other positions are 0.

4.4 Iterative Solution of the System Equations

Solving the system of linear equations using the Newton-Raphson iteration, we assume that after the n th iteration, the residual of Eq. (38) is \mathbf{R}^n . By iterating continuously until convergence, we obtain \mathbf{R}^n as Eq. (39):

$$\mathbf{R}^n = \mathbf{Y} - \mathbf{A}\mathbf{X} - \mathbf{B} \quad (39)$$

For the iteration of the $(n+1)$ th time step and assuming the residual \mathbf{R}^n to be 0, we use Taylor series expansion to get Eq. (40):

$$R^{n+1} = R^n + \left(\frac{\partial R}{\partial x} \right)^n \Delta x = 0 \quad (40)$$

We need to derive Eq. (39), and the formula can be obtained from Eq. (41):

$$\left(\frac{\partial R}{\partial x} \right)^n = -A(T) - B(T)^n \quad (41)$$

Substituting Eq. (41) into Eq. (40), we obtain Eq. (42):

$$(A(T) + B(T)^n)\Delta x = R^n \quad (42)$$

We can find the correction value of the unknown quantity Δx , which can then be expressed as Eq. (43):

$$x^{n+1} = x^n + \lambda \Delta x \quad (43)$$

where λ is the relaxation factor that changes the convergence, and $0 < \lambda \leq 1$. The convergence of iterations can be influenced by changing the relaxation factor.

5 Numerical Examples

5.1 2D Plate Model

We consider a two-dimensional model diagram consisting of a square of 1 m side length on the left and a semicircle of radius 0.5 m on the right side. Additionally, there are adiabatic left and right boundaries, a constant wall temperature of 100 K for the upper boundary, and three boundary conditions of 200 K for the lower boundary with convective heat transfer and convective radiative heat transfer. The material density ρ is 100 kg/m³, specific heat capacity c_p is 100 J/(kg · K), and thermal emissivity h is 100 W/(m² · K). The thermal conductivity of the material as a function of temperature is $k(T) = 15 + 0.01T^2$ W/(m · K), and the boundary element calculation model and the configuration of the interior points are shown in Fig. 3.

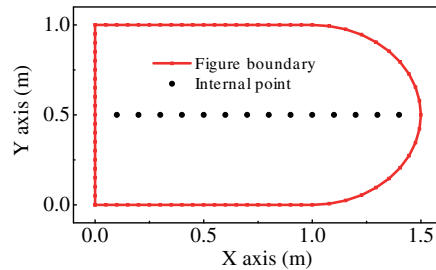


Figure 3: Two-dimensional model with interior points

The original NURBS curve and control point positions are shown in Fig. 4a. The parameter space vector of the boundary element may be produced by normalizing the knot vector, which is written as intervals of [0, 0.25), [0.25, 0.5), [0.5, 0.75), and [0.75, 1), respectively. The new control point sequence, knot vector, and weight factor vector may be produced after refinement by dividing each NURBS element evenly and inserting new knots.

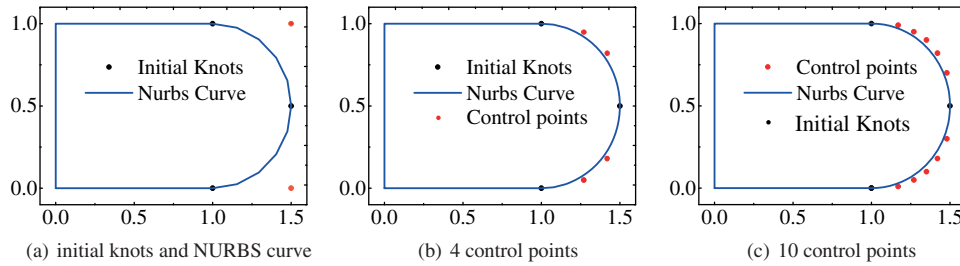


Figure 4: Plate model geometric control points with NURBS curves at various refinement levels, (a) initial knots, (b) 4 control points, (c) 10 control points

Fig. 5a shows the temperature distribution under convective boundary conditions. In the figure, near the heat source at high temperature, the temperature from the lower to upper region increases in accordance with the law of heat transfer. Fig. 5b shows the temperature distribution cloud under temperature boundary conditions. Fig. 5c shows the temperature distribution cloud under convective radiation boundary conditions and it is similar to Fig. 5a, and Fig. 6 shows the temperature of the inner point. When the boundary condition is only temperature-based, the magnitude of the temperature value is proportional to the proximity of the heat source, and when the boundary condition is based on convective or convective radiation, the temperature rises more slowly and the difference between the two is insignificant.

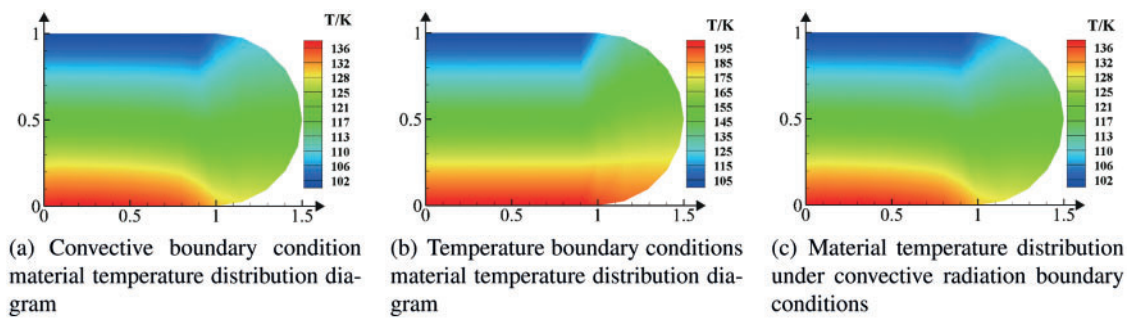


Figure 5: Distribution of homogeneous and non-homogeneous temperature under three conditions of subdivision

Table 3 shows the calculated temperatures of the internal points under different boundary conditions. We provide the calculated temperatures from the IGABEM and FLUENT software on the flat plate boundary. From Table 3 and Fig. 6, we can observe that the IGABEM and FLUENT results have an error of less than 0.7%. Hence, the radial integration method has a high accuracy for solving two-dimensional steady-state nonlinear heat conduction problems. In Fig. 6,

we refer to the temperature boundary conditions as TBC, CHT is the convective heat transfer, and CRHT is the convective radiative heat transfer.

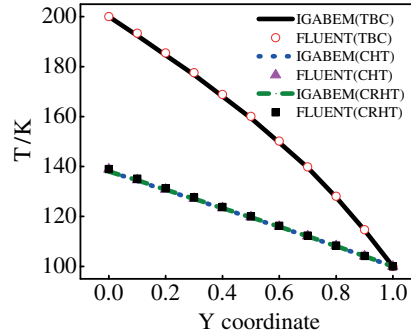


Figure 6: Temperature distribution of flat plate at $x = 0.5$ for different lower boundary conditions

Table 3: Calculated temperatures of points inside 2D graphs with different right boundary conditions

y/m	200 K			Convection heat transfer			Convective radiant heat transfer		
	BEM/K	FLU/K	E/%	BEM/K	FLU/K	E/%	BEM/K	FLU/K	E/%
0	200.00	200.00	0	138.17	138.88	0.51	138.01	138.96	0.69
0.1	192.44	193.38	0.49	134.25	134.57	0.24	134.45	135.09	0.48
0.2	184.61	185.48	0.47	130.54	130.82	0.22	130.72	131.29	0.44
0.3	176.72	177.53	0.46	126.88	127.13	0.20	127.04	127.55	0.40
0.4	168.10	168.83	0.43	123.20	123.41	0.18	123.34	123.78	0.36
0.5	159.40	160.05	0.41	119.51	119.70	0.16	119.64	120.01	0.32
0.6	149.60	150.16	0.37	115.79	115.94	0.13	115.89	116.20	0.27
0.7	139.60	139.82	0.34	111.99	112.11	0.10	112.07	112.31	0.21
0.8	127.69	128.03	0.27	108.10	108.18	0.07	108.16	108.32	0.15
0.9	114.48	114.67	0.17	104.04	104.08	0.04	104.07	104.15	0.08

Now, we consider the temperature boundary condition as an example to study the influence of the number of internal nodes on the accuracy of the calculation results. The number of internal points is considered as 14, 42, 66, and 86 for comparison, as shown in Fig. 7, and the relative error is shown in Fig. 8 and Table 4. It is observed that compared with 86 internal points, the errors of 14 and 42 internal points are larger, with a maximum error of 2.8%, but the calculation result of 66 internal points is very close. Therefore, we can conclude that for smaller number of interior points, there is greater uncertainty in the result, and for larger number of interior points, the temperature value tends to be more stable, which verifies the correctness of the algorithm. Increasing the number of interior points can enhance computation accuracy while simultaneously increasing calculation difficulty. A topic worth investigating is how to choose the number and position of internal points. It's tough to present the determined internal points utilizing a theoretical formulation for this problem's examination. However, uniform distribution works effectively in most cases.

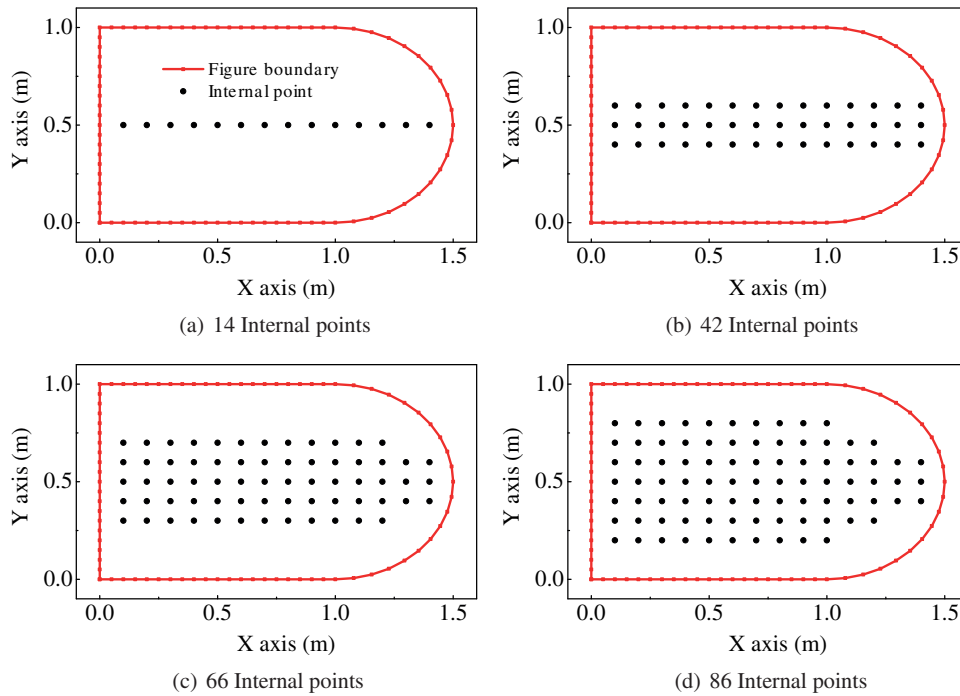


Figure 7: Mesh model with different number of interior points

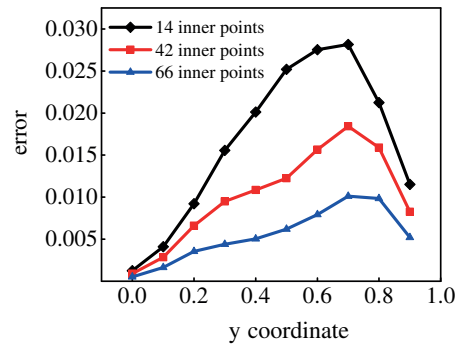


Figure 8: Relative error for models with different number of interior points

Table 4: Calculated temperatures of points inside 2D graphs with different right boundary conditions

y/m	14 inner points			42 inner points			66 inner points		
	BEM/K	86 RESULT	E/%	BEM/K	86 RESULT	E/%	BEM/K	86 RESULT	E/%
0	197.40	197.64	0.12	197.47	197.64	0.09	197.53931	197.64	0.05
0.1	192.16	192.95	0.41	192.40	192.95	0.28	192.63783	192.95	0.16
0.2	184.14	185.86	0.92	184.63	185.86	0.66	185.19521	185.86	0.37
0.3	175.80	178.58	1.56	176.88	178.58	0.95	177.79231	178.58	0.44
0.4	167.20	170.63	2.01	168.78	170.63	1.09	169.76849	170.63	0.50

(Continued)

Table 4 (continued)

y/m	14 inner points			42 inner points			66 inner points		
	BEM/K	86 RESULT	E/%	BEM/K	86 RESULT	E/%	BEM/K	86 RESULT	E/%
0.5	157.96	162.05	2.52	160.06	162.05	1.23	161.04216	162.05	0.62
0.6	148.29	152.48	2.75	150.10	152.48	1.57	151.27515	152.48	0.79
0.7	137.80	141.79	2.82	139.18	141.79	1.84	140.35611	141.79	1.01
0.8	126.66	129.41	2.12	127.36	129.41	1.59	128.13763	129.41	0.99
0.9	114.39	115.72	1.15	114.77	115.72	0.83	115.12064	115.72	0.52

5.2 Rectangular and Semi-Elliptical Models

Let us consider a two-dimensional model diagram of rectangular and semi-elliptical models. The upper region is a rectangle of length 2 m and width 1 m, the lower region is a semi-ellipse and the analytical equation is $x^2 + 4y^2 = 1$ ($y \leq 0$). The domain has adiabatic left and right boundaries, a constant wall temperature of 150 K for the upper boundary, and 100 K for the lower boundary. The material density ρ is 100 kg/m³, and the specific heat capacity c_p is 100 J/(kg · K). The thermal conductivity of the material as a function of temperature is $k(T) = 15 + 0.01T^2$ W/(m · K). The boundary element calculation model is shown in Fig. 9a, and the configuration of the interior points is shown in Fig. 9b. We choose different coefficients of T^2 , and verify the correctness of the algorithm.

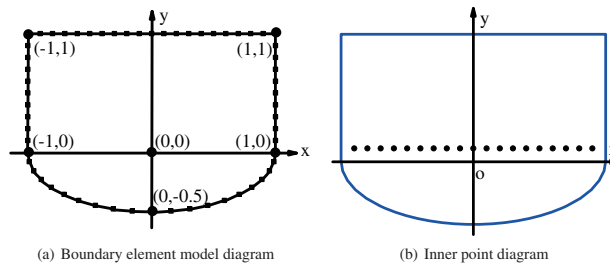
**Figure 9:** Boundary element model and diagram of interior points

Fig. 9a shows the model of the rectangular and semi-ellipse region. We assign the coordinates (1, 0), (1, 1), (-1, 1), (-1, 0), and (0, -0.5) to describe the silhouette of the plate, in order to make the calculation effective. The inner points are shown in Fig. 9b, and the coordinates of the inner points are (-0.9, 0.1), (-0.8, 0.1) ... (0.9, 0.1). There are a total of 19 inner points.

Fig. 10a indicates that the thermal conductivity is a constant value 15 W/(m · K). In the diagram, the right side is a constant 150 K heat source, the left side is a constant 100 K heat source and heat flows from higher to lower temperature values. The left and right temperature trends are basically symmetrical, which conforms to the thermodynamics theorem. As the inhomogeneous coefficient increases, the temperature symmetry changes. For higher temperature value, the thermal conductivity of the material is higher, which leads to an increase in the heat transfer rate and

relatively high temperature values. This can be observed in Fig. 10b and Fig. 10c. In order to better visualize the effect of inhomogeneous thermal conductivity on the variation in temperature values, we present Fig. 11. With constant thermal conductivity, the temperature is lower than that with variable coefficients, and for larger coefficient, the temperature value is larger.

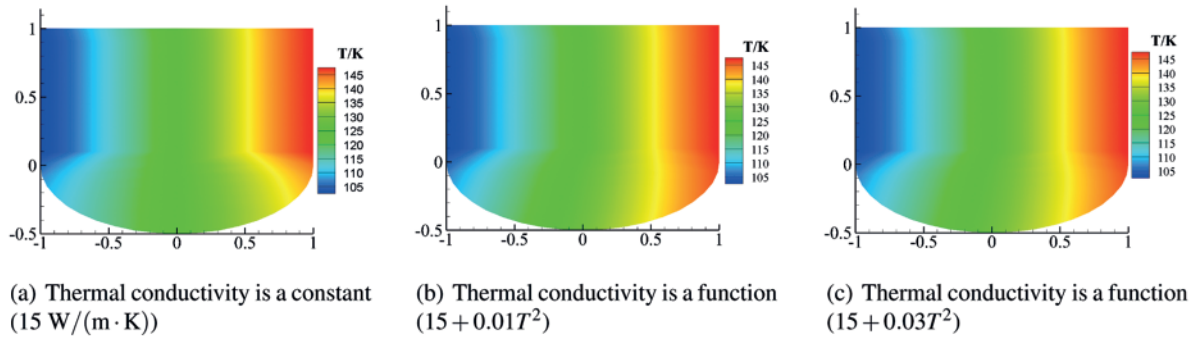


Figure 10: Cloud diagram of the effect of variable thermal conductivity on temperature

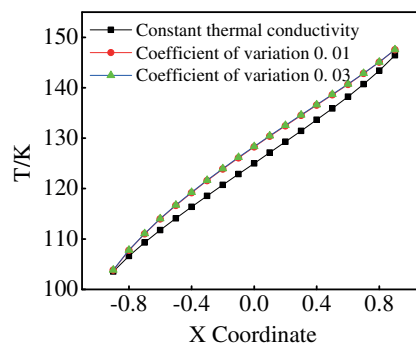


Figure 11: Effect of different coefficients on temperature values

6 Conclusions

In this study, the isogeometric boundary element technique (IGABEM) is applied to solve the two-dimensional non-homogeneous steady state heat conduction problem, and NURBS is used to construct a smooth geometric model. The radial integration method is used to transform the domain integral caused by the variable coefficient into the boundary integral. The numerical results show that the developed algorithm can effectively solve non-homogeneous steady-state heat conduction problems with variable coefficients. In the future, we will extend the algorithm to transient analysis.

Acknowledgement: The authors wish to express their appreciation to the reviewers for their helpful suggestions which greatly improved the presentation of this paper.

Funding Statement: This work is supported by Key Scientific Research Projects of Universities and Key Scientific and Technological Projects in Henan Province, which numbers are 21A440015, 22A570007 and 212102310601, respectively.

Conflicts of Interest: The authors declare that they have no conflicts of interest to report regarding the present study.

References

1. Hughes, T., Cottrell, J., Bazilevs, Y. (2005). Isogeometric analysis: Cad, finite elements, nurbs, exact geometry and mesh refinement. *Computer Methods in Applied Mechanics and Engineering*, 194(39–41), 4135–4195. DOI 10.1016/j.cma.2004.10.008.
2. Cottrell, J., Hughes, T., Reali, A. (2007). Studies of refinement and continuity in isogeometric structural analysis. *Computer Methods in Applied Mechanics and Engineering*, 196(41–44), 4160–4183. DOI 10.1016/j.cma.2007.04.007.
3. Bazilevs, Y., Calo, V., Zhang, Y., Hughes, T. (2006). Isogeometric fluid-structure interaction analysis with applications to arterial blood flow. *Computational Mechanics*, 38(4–5), 310–322. DOI 10.1007/s00466-006-0084-3.
4. Nagy, A., Abdalla, M., Gürdal, Z. (2010). Isogeometric sizing and shape optimisation of beam structures. *Computer Methods in Applied Mechanics and Engineering*, 199(17–20), 1216–1230. DOI 10.1016/j.cma.2009.12.010.
5. Benson, D., Bazilevs, Y., Hsu, M., Hughes, T. (2010). Isogeometric shell analysis: The reissner-mindlin shell. *Computer Methods in Applied Mechanics and Engineering*, 199(5–8), 276–289. DOI 10.1016/j.cma.2009.05.011.
6. de Lorenzis, L., Temizer, Wriggers, P., Zavarise, G. (2011). A large deformation frictional contact formulation using nurbs-based isogeometric analysis. *International Journal for Numerical Methods in Engineering*, 87(13), 1278–1300. DOI 10.1002/nme.3159.
7. Borden, M., Scott, M., Evans, J., Hughes, T. (2010). Isogeometric finite element data structures based on bézier extraction of nurbs. *International Journal for Numerical Methods in Engineering*, 87(1–5), 15–47. DOI 10.1002/nme.2968.
8. Simpson, R., Bordas, S., Trevelyan, J., Rabczuk, T. (2012). A two-dimensional isogeometric boundary element method for elastostatic analysis. *Computer Methods in Applied Mechanics and Engineering*, 209–212, 87–100. DOI 10.1016/j.cma.2011.08.008.
9. Simpson, R., Bordas, S., Lian, H., Trevelyan, J. (2013). An isogeometric boundary element method for elastostatic analysis: 2D implementation aspects. *Computers & Structures*, 118, 2–12. DOI 10.1016/j.compstruc.2012.12.021.
10. Scott, M., Simpson, R., Evans, J., Lipton, S., Bordas, S. et al. (2013). Isogeometric boundary element analysis using unstructured t-splines. *Computer Methods in Applied Mechanics and Engineering*, 254, 197–221. DOI 10.1016/j.cma.2012.11.001.
11. Li, S., Trevelyan, J., Zhang, W., Wang, D. (2018). Accelerating isogeometric boundary element analysis for 3-dimensional elastostatics problems through black-box fast multipole method with proper generalized decomposition. *International Journal for Numerical Methods in Engineering*, 114(9), 975–998. DOI 10.1002/nme.5773.
12. Banerjee, P., Cathie, D. (1980). A direct formulation and numerical implementation of the boundary element method for two-dimensional problems of elasto-plasticity. *International Journal of Mechanical Sciences*, 22(4), 233–245. DOI 10.1016/0020-7403(80)90038-7.
13. Cruse, T. (1996). Bie fracture mechanics analysis: 25 years of developments. *Computational Mechanics*, 18(1), 1–11. DOI 10.1007/BF00384172.
14. Seybert, A., Soenarko, B., Rizzo, F., Shippy, D. (1985). An advanced computational method for radiation and scattering of acoustic waves in three dimensions. *The Journal of the Acoustical Society of America*, 77(2), 362–368. DOI 10.1121/1.391908.

15. Nguyen, B., Tran, H., Anitescu, C., Zhuang, X., Rabczuk, T. (2016). An isogeometric symmetric galerkin boundary element method for two-dimensional crack problems. *Computer Methods in Applied Mechanics and Engineering*, 306, 252–275. DOI 10.1016/j.cma.2016.04.002.
16. Peng, X., Atroshchenko, E., Kerfriden, P., Bordas, S. P. A. (2017). Linear elastic fracture simulation directly from CAD: 2D nurbs-based implementation and role of tip enrichment. *International Journal of Fracture*, 204(1), 55–78. DOI 10.1007/s10704-016-0153-3.
17. Peng, X., Atroshchenko, E., Kerfriden, P., Bordas, S. P. A., Peng, X. et al. (2017). Isogeometric boundary element methods for three dimensional static fracture and fatigue crack growth. *Computer Methods in Applied Mechanics and Engineering*, 316, 151–185. DOI 10.1016/j.cma.2016.05.038.
18. Chen, L., Wang, Z., Peng, X., Yang, J., Wu, P. et al. (2021). Modeling pressurized fracture propagation with the isogeometric bem. *Geomechanics and Geophysics for Geo-Energy and Geo-Resources*, 7(3), 51. DOI 10.1007/s40948-021-00248-3.
19. Simpson, R., Liu, Z., Vázquez, R., Evans, J. (2018). An isogeometric boundary element method for electromagnetic scattering with compatible B-spline discretizations. *Journal of Computational Physics*, 362, 264–289. DOI 10.1016/j.jcp.2018.01.025.
20. Simpson, R., Scott, M., Taus, M., Thomas, D., Lian, H. (2014). Acoustic isogeometric boundary element analysis. *Computer Methods in Applied Mechanics and Engineering*, 269, 265–290. DOI 10.1016/j.cma.2013.10.026.
21. Peake, M., Trevelyan, J., Coates, G. (2015). Extended isogeometric boundary element method (xibem) for three-dimensional medium-wave acoustic scattering problems. *Computer Methods in Applied Mechanics and Engineering*, 284, 762–780. DOI 10.1016/j.cma.2014.10.039.
22. Keuchel, S., Hagelstein, N., Zaleski, O., VonÁ estorff, O. (2017). Evaluation of hypersingular and nearly singular integrals in the isogeometric boundary element method for acoustics. *Computer Methods in Applied Mechanics and Engineering*, 325, 488–504. DOI 10.1016/j.cma.2017.07.025.
23. Chen, L., Marburg, S., Zhao, W., Liu, C., Chen, H. (2019). Implementation of isogeometric fast multipole boundary element methods for 2D half-space acoustic scattering problems with absorbing boundary condition. *Journal of Theoretical and Computational Acoustics*, 27(2), 1850024. DOI 10.1142/S259172851850024X.
24. Chen, L., Lian, H., Liu, Z., Chen, H., Atroshchenko, E. et al. (2019). Structural shape optimization of three dimensional acoustic problems with isogeometric boundary element methods. *Computer Methods in Applied Mechanics and Engineering*, 355, 926–951. DOI 10.1016/j.cma.2019.06.012.
25. Chen, L., Liu, C., Zhao, W., Liu, L. (2018). An isogeometric approach of two dimensional acoustic design sensitivity analysis and topology optimization analysis for absorbing material distribution. *Computer Methods in Applied Mechanics and Engineering*, 336, 507–532. DOI 10.1016/j.cma.2018.03.025.
26. Jiang, F., Zhao, W., Chen, L., Zheng, C., Chen, H. (2021). Combined shape and topology optimization for sound barrier by using the isogeometric boundary element method. *Engineering Analysis with Boundary Elements*, 124, 124–136. DOI 10.1016/j.enganabound.2020.12.009.
27. Chen, L., Lu, C., Zhao, W., Chen, H., Zheng, C. (2020). Subdivision surfaces-boundary element accelerated by fast multipole for the structural acoustic problem. *Journal of Theoretical and Computational Acoustics*, 28(2), 2050011. DOI 10.1142/S2591728520500115.
28. Zhao, W., Chen, L., Chen, H., Marburg, S. (2020). An effective approach for topological design to the acoustic-structure interaction systems with infinite acoustic domain. *Structural and Multidisciplinary Optimization*, 62, 1253–1273. DOI 10.1007/s00158-020-02550-2.
29. Chen, L., Zhang, Y., Lian, H., Atroshchenko, E., Ding, C. et al. (2020). Seamless integration of computer-aided geometric modeling and acoustic simulation: Isogeometric boundary element methods based on catmull-clark subdivision surfaces. *Advances in Engineering Software*, 149, 102879. DOI 10.1016/j.advengsoft.2020.102879.
30. Li, K., Qian, X. (2011). Isogeometric analysis and shape optimization via boundary integral. *Computer-Aided Design*, 43(11), 1427–1437. DOI 10.1016/j.cad.2011.08.031.

31. Lian, H., Kerfriden, P., Bordas, S. (2016). Implementation of regularized isogeometric boundary element methods for gradient-based shape optimization in two-dimensional linear elasticity. *International Journal for Numerical Methods in Engineering*, 106(12), 972–1017. DOI 10.1002/nme.5149.
32. Lian, H., Kerfriden, P., Bordas, S. (2017). Shape optimization directly from cad: An isogeometric boundary element approach using T-splines. *Computer Methods in Applied Mechanics and Engineering*, 317, 1–41. DOI 10.1016/j.cma.2016.11.012.
33. Liu, C., Chen, L., Zhao, W., Chen, H. (2017). Shape optimization of sound barrier using an isogeometric fast multipole boundary element method in two dimensions. *Engineering Analysis with Boundary Elements*, 85, 142–157. DOI 10.1016/j.enganabound.2017.09.009.
34. Chen, L., Lu, C., Lian, H., Liu, Z., Zhao, W. et al. (2020). Acoustic topology optimization of sound absorbing materials directly from subdivision surfaces with isogeometric boundary element methods. *Computer Methods in Applied Mechanics and Engineering*, 362, 112806. DOI 10.1016/j.cma.2019.112806.
35. Chen, L., Lian, H., Liu, Z., Gong, Y., Zheng, C. et al. (2022). Bi-material topology optimization for fully coupled structural-acoustic systems with isogeometric fem-bem. *Engineering Analysis with Boundary Elements*, 135, 182–195. DOI 10.1016/j.enganabound.2021.11.005.
36. Mierzwiczak, M., Chen, W., Fu, Z. J. (2015). The singular boundary method for steady-state nonlinear heat conduction problem with temperature-dependent thermal conductivity. *International Journal of Heat and Mass Transfer*, 91, 205–217. DOI 10.1016/j.ijheatmasstransfer.2015.07.051.
37. Gao, X., Wang, J. (2009). Interface integral bem for solving multi-medium heat conduction problems. *Engineering Analysis with Boundary Elements*, 33(4), 539–546. DOI 10.1016/j.enganabound.2008.08.009.
38. Gao, X. (2006). A meshless bem for isotropic heat conduction problems with heat generation and spatially varying conductivity. *International Journal for Numerical Methods in Engineering*, 66(9), 1411–1431. DOI 10.1002/nme.1602.
39. Gong, Y., Trevelyan, J., Hattori, G., Dong, C. (2019). Hybrid nearly singular integration for isogeometric boundary element analysis of coatings and other thin 2D structures. *Computer Methods in Applied Mechanics and Engineering*, 346, 642–673. DOI 10.1016/j.cma.2018.12.019.
40. Gong, Y., Yang, H., Dong, C. (2018). A novel interface integral formulation for 3D steady state thermal conduction problem for a medium with non-homogenous inclusions. *Computational Mechanics*, 63(2), 181–199. DOI 10.1007/s00466-018-1590-9.
41. An, Z., Yu, T., Bui, T., Wang, C., Trinh, N. (2018). Implementation of isogeometric boundary element method for 2-D steady heat transfer analysis. *Advances in Engineering Software*, 116, 36–49. DOI 10.1016/j.advengsoft.2017.11.008.
42. Yu, B., Zhou, H. L., Chen, H. L., Tong, Y. (2015). Precise time-domain expanding dual reciprocity boundary element method for solving transient heat conduction problems. *International Journal of Heat and Mass Transfer*, 91, 110–118. DOI 10.1016/j.ijheatmasstransfer.2015.07.109.
43. Cui, M., Peng, H. F., Xu, B. B., Gao, X. W., Zhang, Y. (2018). A new radial integration polygonal boundary element method for solving heat conduction problems. *International Journal of Heat and Mass Transfer*, 123, 251–260. DOI 10.1016/j.ijheatmasstransfer.2018.02.111.
44. Yu, B., Yao, W. A., Gao, X. W., Zhang, S. (2014). Radial integration bem for one-phase solidification problems. *Engineering Analysis with Boundary Elements*, 39, 36–43. DOI 10.1016/j.enganabound.2013.10.018.
45. Yu, B., Cao, G., Huo, W., Zhou, H., Atroshchenko, E. (2021). Isogeometric dual reciprocity boundary element method for solving transient heat conduction problems with heat sources. *Journal of Computational and Applied Mathematics*, 385, 113197. DOI 10.1016/j.cam.2020.113197.
46. Mostafa Shaaban, A., Anitescu, C., Atroshchenko, E., Rabczuk, T. (2020). Shape optimization by conventional and extended isogeometric boundary element method with pso for two-dimensional helmholtz acoustic problems. *Engineering Analysis with Boundary Elements*, 113, 156–169. DOI 10.1016/j.enganabound.2019.12.012.
47. Zhao, W., Chen, L., Chen, H., Marburg, S. (2019). Topology optimization of exterior acoustic-structure interaction systems using the coupled FEM-BEM method. *International Journal for Numerical Methods in Engineering*, 119(5), 404–431. DOI 10.1002/nme.6055.